ACS APPLIED MATERIALS & INTERFACES

www.acsami.org

Research Article

Double-Exchange Bias Modulation under Horizontal and Perpendicular Field Directions by 3D Nanocomposite Design

Jijie Huang,* Di Zhang, Juncheng Liu, Hongyi Dou, and Haiyan Wang*

Cite This: *ACS Appl. Mater. Interfaces* 2021, 13, 50141−50148

Read Online

ACCESS | Metrics & More | Article Recommendations | Supporting Information

ABSTRACT: Exchange bias (EB) presents the interfacial coupling between ferromagnetic (FM) and antiferromagnetic (AFM) phases, which could be applied for high-density data storage and magnetic recording. In thin films, the EB effect could be realized in either a FM/AFM multilayer structure or a FM/AFM vertically aligned nanocomposite (VAN) form, which allows the interfacial coupling tuning along the horizontal or perpendicular directions, respectively. Here, to combine the schemes of multilayer and VAN structures, a new 3D nanocomposite has been designed, which is $La_{0.7}Sr_{0.3}MnO_3$ (LSMO)/NiO VAN layers with inserted LSMO or NiO layers. Such a 3D nanocomposite structure provides a great platform to tailor the EB effect along both horizontal and perpendicular directions. Specifically, the sample with a NiO interlayer exhibits the highest EB field (H_{EB}) of 350 Oe and 475 Oe under in-plane and out-of-plane field, respectively. Furthermore, the H_{EB} value and Curie temperature (T_c) can be tuned by different 3D nanostructures. This work demonstrates the double EB modulation with the designed 3D nanostructures as a new route toward advanced magnetic data storage and spintronic devices.

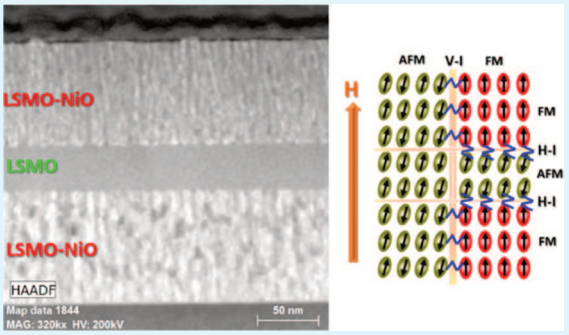

KEYWORDS: *exchange bias, 3D nanocomposite thin film, vertically aligned nanocomposite, magnetic property, multilayer*

INTRODUCTION

Exchange bias (EB) effect presents the shift of the hysteresis loop of the ferromagnetic (ferrimagnetic, FM)/antiferromagnetic (AFM) heterostructure while cooling through the Néel temperature (T_N) of the AFM phase. The EB field is defined as $H_{EB} = |H_+ + H_-|/2$, where H_+ and H_- are the positive and negative coercivities in the hysteresis loop, respectively. The EB effect can be employed in various applications, such as magnetic data storage, spin valve devices, magnetic sensors, magnetic hard disk heads, and spintronic applications.[1−5] The EB effect has been realized in different nanostructures with FM/AFM interfacial exchange coupling, among which thin-film geometry is ideal for practical applications. Conventionally, the EB effect can be achieved by FM/AFM multilayers, which alternatively stack the FM layer and AFM layer. Various material systems have been adopted to obtain such multilayers with an EB effect, such as the Co/CuMn (metal/alloy bilayer),[6] Fe/FeO (metal/oxide bilayer),[7] $La_{0.7}Sr_{0.3}MnO_3$ (LSMO)/$BiFeO_3$ (BFO) (oxide/oxide bilayer),[8] Co/CoO/Co (metal/oxide/metal trilayer),[9] and $LaNiO_3/LaMnO_3$ superlattices.[10]

In such a multilayer structure, the interfacial exchange coupling occurs at the transverse FM/AFM interface (i.e., lateral interface), which makes the EB effect more evident with a horizontal applied magnetic field (horizontal EB effect). Furthermore, the H_{EB} value in the multilayer can be tuned by controlling the layer number and the thickness of the FM layer (t_{FM}). For example, it was found that EB is inversely proportional to the FM layer thickness ($H_{EB} \propto 1/t_{FM}$), which suggests that a lower thickness of the FM layer is preferred to achieve a high H_{EB} value.[11] On the other hand, perpendicular EB effect is considered to be easier to achieve high-density magnetic data storage and is more thermal stable in local areas.[12,13] Although the perpendicular EB effect can be realized in multilayers by introducing a magnetic anisotropic FM layer (such as CoPt alloy or Co/Pt multilayer), the choice of magnetic anisotropic FM material is limited.[14,15] Recently, vertically aligned nanocomposite (VAN) thin films provide a great platform to create a heterointerface along the vertical direction, which allows physical property manipulation in an unconventional way.[16−18] Pronounced perpendicular EB effect has been observed in several VAN systems, such as LSMO/NiO, LSMO/$LaFeO_3$, NiO/$NiFe_2O_4$, LSMO/BFO, and so forth.[19−22] Furthermore, such VANs have even been integrated on Si and flexible mica substrates with comparable H_{EB} values as those of the films deposited on single-crystal substrates.[23,24] Overall, the multilayer and VAN structures allow the EB effect

Received: August 3, 2021
Accepted: October 5, 2021
Published: October 13, 2021

https://doi.org/10.1021/acsami.1c14699
ACS Appl. Mater. Interfaces 2021, 13, 50141−50148

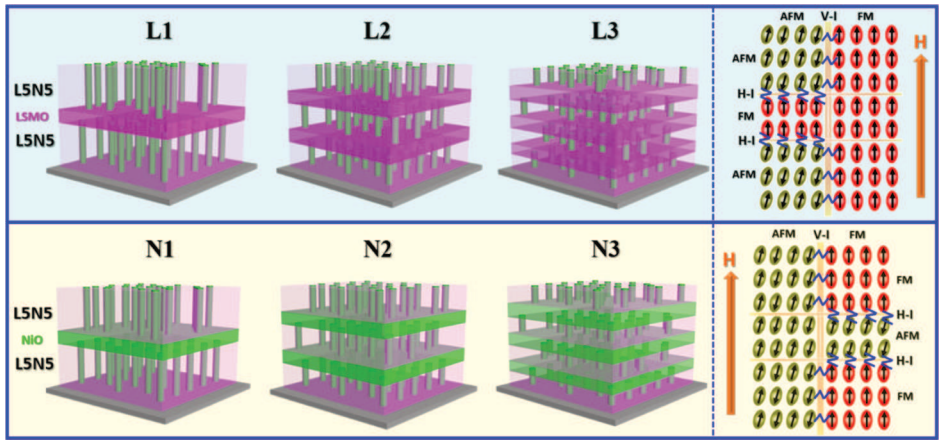

Figure 1. Schematic illustration of the 3D nanocomposite thin-film design with different interlayers and different numbers of interlayers; right panel is the interfacial exchange coupling along both horizontal and perpendicular interfaces.

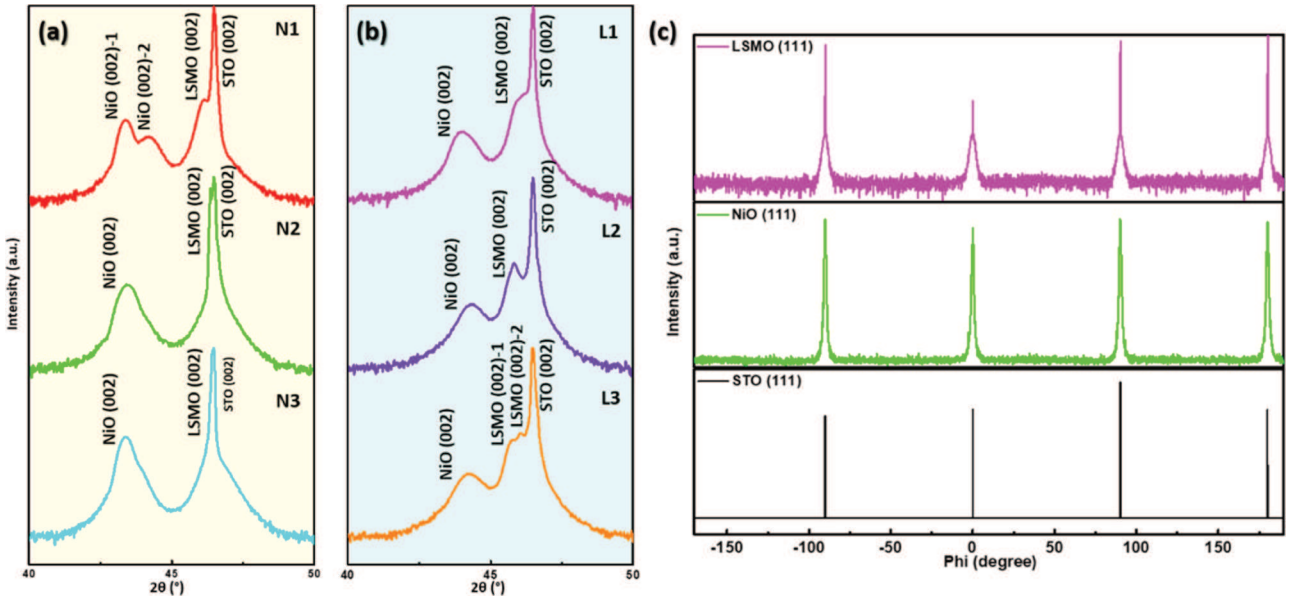

Figure 2. Standard θ−2θ XRD scans of (a) N1, N2, and N3 series samples and (b) L1, L2, and L3 series samples; (c) phi-scan of LSMO (111), NiO (111), and STO (111) peaks on the N1 sample.

in the horizontal and perpendicular field directions, respectively. However, tailoring the EB properties in both directions using one material system remains very challenging, considering the exclusive nature of magnetic anisotropy.

In this work, we adopted the concepts of both multilayer and VAN structures and designed a VAN-multilayer combined 3D nanocomposite structure for tailoring the EB properties in both horizontal and perpendicular directions, as shown in the schematic illustration in Figure 1. In such a design, $LSMO_{0.5}$/$NiO_{0.5}$ VAN (simplified as L5N5 hereafter) has been selected as a model system, and two series of films with either LSMO- or NiO-interlayers were grown with different numbers of interlayers, and the samples L1, L2, or L3 and N1, N2, or N3 refer to 1, 2, or 3 LSMO or NiO interlayers, respectively. In such a 3D nanocomposite structure, FM/AFM interfacial exchange coupling could exist in both horizontal and perpendicular directions, as illustrated in the right panel of Figure 1, which allows the manipulation of both horizontal and perpendicular EB effects.

RESULTS AND DISCUSSION

Standard θ−2θ X-ray diffraction (XRD) scans were first characterized and are plotted in Figure 2a for N1−N3 and Figure 2b for L1−L3; only NiO (002) and LSMO (002) peaks were identified for all 3D nanocomposite thin films, which indicates the highly textured growth of the films. The c-lattice parameters of NiO and LSMO phases in all samples can be calculated, and the results are summarized in Table 1 along with the corresponding out-of-plane (OP) strain, which is calculated by $\varepsilon = \frac{d_{film} - d_{bulk}}{d_{bulk}}$. The OP strains of both NiO and LSMO are varied in different films; basically, NiO undergoes OP compressive strain, and OP tensile strain is exerted in LSMO, which suggests the lattice coupling in the vertical LSMO/NiO interface. Interestingly, two NiO (002) peaks were observed in the N1 sample; refer to the lattice parameter of the NiO phase in the VAN layers and the NiO interlayer. Similar results were obtained for the LSMO (002) peaks in the L3 sample, while all other samples present one peak for each phase. This is attributed to the difference of the elastic

https://doi.org/10.1021/acsami.1c14699
ACS Appl. Mater. Interfaces 2021, 13, 50141−50148

Table 1. *c*-Lattice Parameter and OP Strain of Both NiO and LSMO Phases in All Samples

samples	NiO *c*-lattice parameter (Å)	NiO OP strain	LSMO *c*-lattice parameter (Å)	LSMO OP strain
N1	4.169/4.095	−0.02/−1.80	3.931	1.42
N2	4.162	−0.19	3.913	0.95
N3	4.169	−0.02	3.905	0.75
L1	4.115	−1.32	3.929	1.37
L2	4.085	−2.04	3.958	2.12
L3	4.094	−1.82	3.939/3.962	1.63/2.22
bulk	4.17		3.876	

modulus in the LSMO and NiO phases, for example E_{LSMO} is ∼562 GPa[25], and E_{NiO} is ∼185 GPa,[26] and therefore, the lattice of NiO is easier to be distorted compared to LSMO. For sample N1, two NiO (002) peaks refer to the NiO interlayer and VAN layer; for N2 and N3, the thickness of each VAN layer is smaller, so NiO phase in the VAN layer prefers to follow the lattice of the NiO interlayer and thus one NiO peak formed. In comparison, for L1 and L2, only one LSMO peak appears as its lattice is rigid. However, for L3, two LSMO peaks form as more LSMO/NiO interface forms and the lattice strain starts to influence the LSMO phase. Strain is a considerable factor for tailoring the H_{EB} value, for example, the tensile strain in LSMO can stabilize the spins and consequently enhance the H_{EB} value.[27] Furthermore, for NiO, the in-plane (IP) compressive strain (or OP tensile strain) results in the tendency of the transverse rotation of the AFM spins,[28] while IP tensile strain (or OP compressive strain) leads to the tendency of vertical rotation of the AFM spins.[29] The detailed magnetic properties of the different 3D nanocomposite thin films will be discussed in the following section. Figure 2c presents the phi-scan of LSMO (111), NiO (111), and $SrTiO_3$ (STO) (111) peaks of the selected N1 sample; all of them exhibit four sharp peaks with 90° interval, which indicates the cube-on-cube growth of both LSMO and NiO phases as well as the excellent crystal quality of the VAN multilayer film. The phi-scan of LSMO (111), NiO (111), and STO (111) peaks of the L2 sample shown in Figure S1 further proves the high quality of the 3D films with either NiO or LSMO interlayers. The rocking curves of all samples have also been measured to explore the crystallinity of NiO and LSMO phases in all samples, as shown in Figures S2 and S3 for N-series and L-series samples, and the full width at half-maximum (fwhm) of all peaks are listed in Table S1. Several features can be observed. First, fwhm of the LSMO (002) peak is smaller than that of the NiO (002) peak, which is because LSMO has a

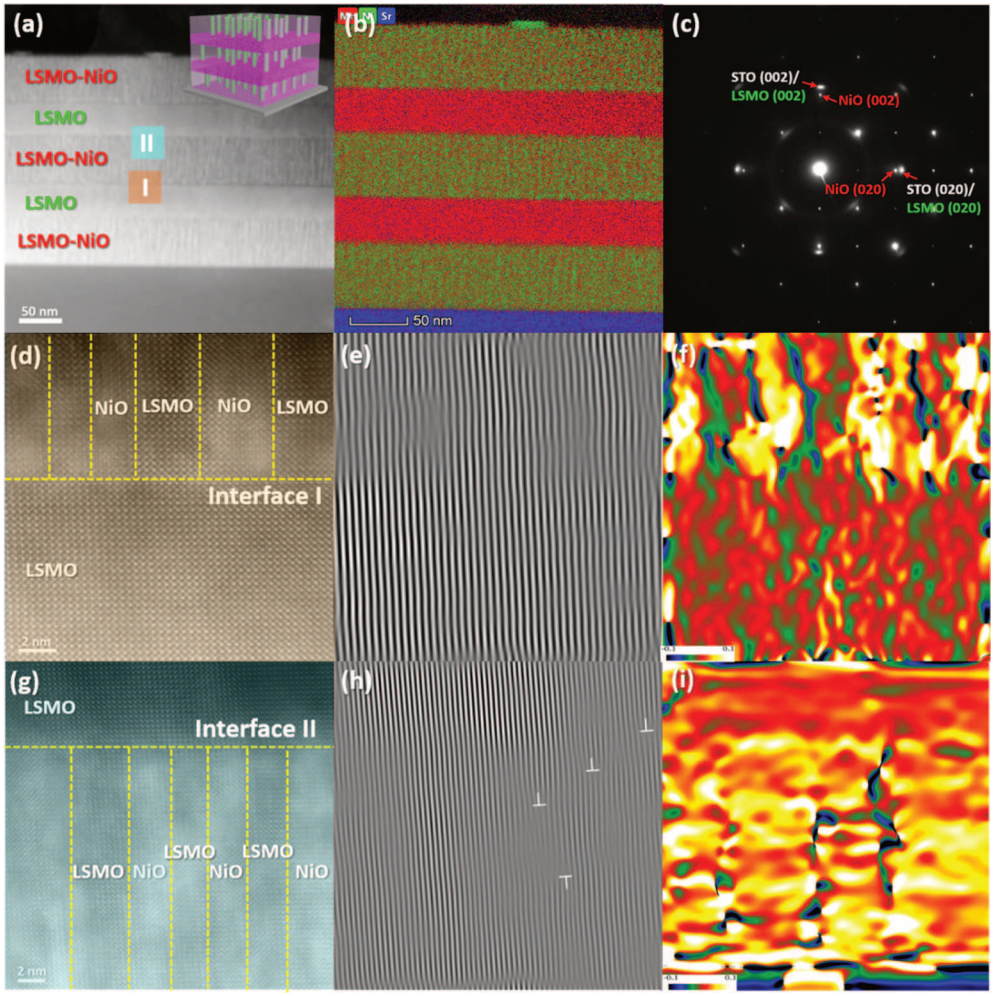

Figure 3. Detailed microstructure study on sample L2. (a) Low-mag STEM image with corresponding (b) EDX mapping and (c) SAED pattern taken in the STO [100] zone axis; (d) high-resolution STEM image of interface I with corresponding (e) IFFT image and (f) GPA mapping; (g) high-resolution STEM image of interface II with corresponding (h) IFFT image and (i) GPA mapping.

https://doi.org/10.1021/acsami.1c14699
ACS Appl. Mater. Interfaces 2021, 13, 50141−50148

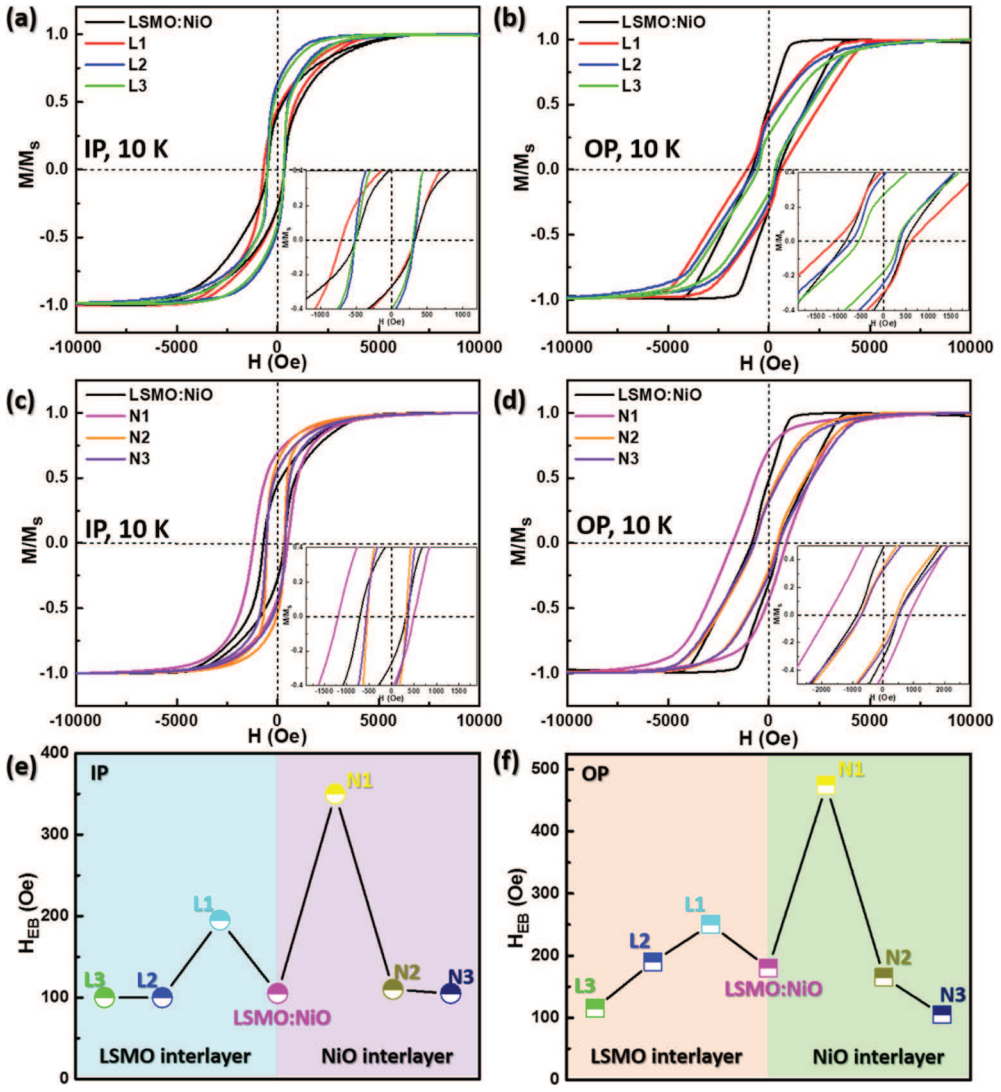

Figure 4. Magnetization hysteresis loops of all samples under different conditions. L series samples under (a) IP and (b) OP fields at 10 K; N series samples under (c) IP and (d) OP fields at 10 K; the insets are the enlarged area to estimated H_{EB} values; the calculated H_{EB} values are compared (e) for the IP field and (f) for the OP field.

better lattice matching with the STO substrate (note that the rocking curves of LSMO (002) in samples N2 and N3 are missing as they are fully overlapped with the STO (002) peak). Furthermore, for the NiO (002) peak in the N-series samples, fwhm becomes smaller with more NiO interlayers, which suggests that the NiO interlayer is the main factor to contribute to the rocking curve. On the other hand, for the NiO (002) peak in the L-series samples, fwhm becomes larger with more LSMO interlayers, which is because NiO phase only exists in the VAN layers and its crystallinity gets worse with more LSMO interlayers.

To further explore the film quality, detailed transmission electron microscopy (TEM) study has been conducted on the L2 sample. Figure 3a,b shows the low-mag scanning TEM (STEM) image and its corresponding energy-dispersive X-ray spectroscopy (EDX) mapping; the thickness of the VAN layer and the inserted LSMO layer can be estimated as 60 and 40 nm, respectively, and the interface between each layer is relatively smooth. The VAN layer exhibits a typical nanopillar-in-matrix structure, that is, NiO nanopillars embedded into the LSMO matrix. The selected area electron diffraction (SAED) pattern taken in the STO [100] zone axis is shown in Figure 3c, and the distinguished NiO (002) and LSMO (002) diffraction dots indicate the perfect OP alignment of the two phases in the film. Then, high-resolution STEM images were taken at interface I and interface II as marked in Figure 3a. The high-resolution STEM of interface I is shown in Figure 3d with its corresponding inverse fast Fourier transform (IFFT) image in Figure 3e. A nearly perfect lattice with very few defects is obtained. The lattice mismatch has been compensated by the interfacial strain, as displayed in the geometric phase analysis (GPA) map in Figure 3f. Tensile and compressive strains can be identified in the LSMO phase (inserted layer or inside the VAN layer) and NiO phase, respectively, which is consistent with the above XRD results. Furthermore, the high-resolution STEM and corresponding IFFT images of interface II are presented in Figure 3g,h, respectively. More dislocations are observed at the interface area compared to interface I as the film quality is slightly degraded with more layers. The GPA map in the same area again demonstrates the tensile strain in LSMO and the compressive strain in NiO, as shown in Figure 3i. The low-mag STEM image and the corresponding EDX

https://doi.org/10.1021/acsami.1c14699
ACS Appl. Mater. Interfaces 2021, 13, 50141−50148

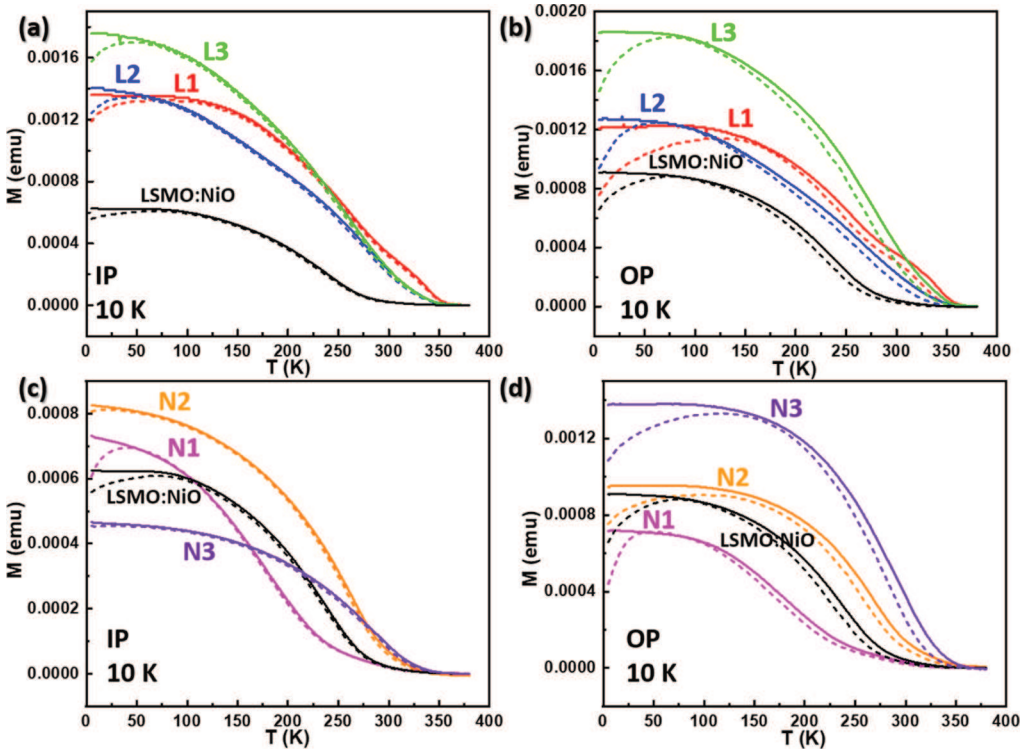

Figure 5. Temperature dependence of ZFC and FC magnetization of all 3D nanocomposite thin films compared with the LSMO/NiO single layer film. $M-T$ curves of the L series samples under (a) IP and (b) OP fields at 10 K; $M-T$ curves of the N series samples under (c) IP and (d) OP fields at 10 K.

mapping of sample L1 is also shown in Figure S4. The microstructure of the N series samples of N1 and N2 presents a very similar 3D structure with NiO interlayers, as shown in Figures S5 and S6, respectively. Overall, the 3D nanocomposite thin film presents excellent crystallinity with different strain conditions in each phase, while the film quality degrades with more layers grown.

Next, we focus on the magnetic properties of these 3D nanocomposite thin films. First, the magnetization hysteresis loops were measured for all samples with the applied magnetic field (from −10 000 Oe to 10 000 Oe) in the IP (parallel to the film surface) or OP (perpendicular to the film surface) direction at 10 K. Figure 4a−d plots the hysteresis loops of L1−L3 under IP field and OP field and of N1−N3 under IP field and OP field, respectively. The insets in each figure are the enlarged area to estimate the EB H_{EB} values, which is compared in Figure 4e,f for IP and OP, respectively. The data for the single layer of LSMO/NiO was also included as the reference. All of the samples show an obvious EB effect with H_{EB} values higher than 100 Oe, and the 3D nanocomposite thin films with one inserted interlayer (L1, N1) obtain the highest H_{EB} values under both IP and OP fields. The variation of the H_{EB} values in different samples could be attributed to the combined effect of the different strain states and the film quality degradation with more layers, as mentioned above. Among them, N1 obtains the highest H_{EB} values of 350 Oe and 475 Oe under IP and OP fields, which is much higher than that of the LSMO/NiO single-layer film. On comparing sample N1 with sample L1, the same amount of LSMO/NiO vertical interface is generated in both films; however, more LSMO/NiO horizontal interface is formed in sample N1 as LSMO is the matrix in the VAN layer, which results in higher H_{EB} values in sample N1. Another interesting finding is that the OP H_{EB} values are higher than the IP H_{EB} values for most of the samples, which probably results from the large amount of vertical interface in the VAN layers. Overall, the EB effect in both directions can be effectively enhanced by such a 3D nanostructure design. Further tuning could be realized by controlling the thickness of the interlayers or the VAN layer, composition variation of the VAN layer, or developing other VAN systems.

Last, the temperature-dependent magnetization ($M-T$, 5 to 380 K) measurements under field cooling (FC, 1000 Oe, IP or OP) and zero-FC (ZFC) conditions have been carried out for all samples, and the results are shown in Figure 5. One major finding is that the Curie temperature (T_c, paramagnetic to ferromagnetic transition point) of LSMO in all of the 3D nanocomposite thin films is higher than that of the LSMO/NiO single layer (with IP or OP field), which is related to the strain state in each film. All of them obtain lower T_c compared to the previously reported pure LSMO of ∼370 K.[30] Generally, the magnetic response of LSMO is highly dependent on the double exchange of the e_g hopping from Mn^{3+} to Mn^{4+}, and the modification of the angle or length of the Mn−O−Mn bond caused by strain can correspondingly tailor its magnetic performance. It was reported that IP compressive strain results in higher T_c because of the reduced Mn−O−Mn bond length, while oppositely, tensile strain leads to lower T_c.[31,32] In addition, defects such as oxygen vacancies could break the exchange mechanism and increase the spin disorder and thus reduce T_c.[33] Therefore, the mechanism of the increased T_c in this case is quite complicated as both the strain state and the interfacial defects could contribute to the magnetic properties. Another finding is that the magnetization monotonically decreases with increasing temperature in the FC curves, while in the ZFC curves, the magnetization gradually increases

https://doi.org/10.1021/acsami.1c14699
ACS Appl. Mater. Interfaces 2021, 13, 50141−50148

to the maximum value (blocking temperature: T_B) and then continuously decreases with increasing temperature. Interestingly, a bifurcation between the FC and ZFC curves can be observed for all samples at different temperatures (irreversible temperature T_{irr}, as compared and shown in Figuer S7 for all samples), which suggests that the lack of magnetic ordering under such a temperature and LSMO phase might turn into spin-glass, spin clusters, or superparamagnets. Several factors might be responsible for the varied T_{irr}, such as the finite-size effect due to the ultrafine NiO nanopillars,[34] as well as the magnetic disorder caused by interfacial defects.[35] Overall, the magnetic states in the 3D nanocomposite thin films are relatively complicated because of the complex strain states and interfacial effect, and further investigations are needed to fully understand the tuning mechanism.

Several approaches have been previously reported to tailor the EB effect, such as the thickness variation of the AFM layer[36] or FM layer,[11] the spin structure of the FM phase,[37] spin−orbit torque,[38] strain,[39] and so forth. For the conventional multilayer or VAN films, the FM/AFM interface is generated either in the horizontal or vertical direction, which limits the tunability of the EB effect. The 3D nanocomposite thin films in this work provide a new way for EB effect tuning in both horizontal and vertical directions by architecture design, though the exact tuning mechanism is still under further investigation in the complex structure. The results in this work present effective H_{EB} tuning on the 3D nanocomposite thin films. For future perspective, further tuning can be achieved by controlling the thickness of each layer, composition variation of the VAN layer, and others. Besides the EB property tuning, 3D nanocomposite design could be employed for magnetotransport (e.g., low-field magneto resistance properties)[40] or plasmonic properties tuning.[41] Furthermore, such a 3D nanocomposite concept could be adopted for other unexplored systems for property tailoring, such as 3D ionic conductivity channels, 3D strain for enhanced ferroelectricity, and so forth.

CONCLUSIONS

A new 3D nanocomposite thin film with combined VAN and multilayer structures has been grown for EB effect modulation in both horizontal and perpendicular field directions. More specifically, the 3D nanocomposites include LSMO/NiO VAN layers inserted by one, two, or three layers of LSMO (L1, L2, L3) or NiO (N1, N2, N3) layers. The VAN multilayers show epitaxial growth with excellent film quality despite the complicated 3D structures. All of the films show enhanced H_{EB} values, with the N1 sample obtaining the highest H_{EB} values of 350 Oe and 475 Oe under IP and OP fields, and the H_{EB} values could be tailored by controlling the inserted layer and the layer number. In addition, other magnetic properties such as the Curie temperature T_c, blocking temperature T_B, and irreversible temperature T_{irr} are also tunable. The VAN multilayer structure provides design flexibility for interfacial modulation and strain state control and thus tailorable magnetic properties, pending exact tuning mechanism under further investigation.

EXPERIMENTAL SECTION

The LSMO, NiO, and $(LSMO)_{0.5}(NiO)_{0.5}$ targets were made by conventional solid-state mixing; the mixed powders were then pressed into a pellet (1 in. diameter) followed by a sintering process under 1200 °C for 6 h. All of the thin films were deposited on STO (001) substrates using the pulsed laser deposition technique with a KrF excimer laser (Lambda Physik, λ = 248 nm). The 3D structures were obtained by alternative deposition of the $(LSMO)_{0.5}(NiO)_{0.5}$ target and the LSMO or NiO target. More specifically, 3000 pulses were deposited for each VAN layer in sample N1, 2000 pulses were used for each VAN layer in sample N2, and 1500 pulses for each VAN layer in sample N3. One thousand pulses were fixed for LSMO or NiO interlayers in all samples. Before deposition, the base pressure was below 1×10^{-6} Torr. During deposition, the substrate temperature was raised to 700 °C with 100 mTorr O_2 inflowing, and the deposition frequency was set at 5 Hz. The target−substrate distance was fixed at 4.5 cm. After deposition, the samples were cooled down at 10 °C/min in 200 Torr O_2.

The crystal structure of the films was characterized by XRD (Panalytical X'Pert X-ray diffractometer). High-angle annular dark α field STEM images were collected on an aberration-corrected FEI Themis Z microscope, while EDX chemical mapping was taken by a FEI Talos F200X transmission electron microscope. The TEM samples were prepared using the conventional mechanical method, including grinding, dimpling, and ion milling (PIPS 695). Temperature dependence magnetization (2−380 K) and magnetic hysteresis loops (from −10 000 Oe to 10 000 Oe) were measured by a SQUID magnetometer (MPMS: Quantum Design), with the applied field in the direction of either perpendicular or parallel to the film surface.

ASSOCIATED CONTENT

Supporting Information

The Supporting Information is available free of charge at https://pubs.acs.org/doi/10.1021/acsami.1c14699.

Phi-scan of LSMO (111), NiO (111), and STO (111) peaks on the L2 sample; rocking curves of all samples; and low-mag STEM image with corresponding EDX mapping of samples L1, N1, and N2 (PDF)

AUTHOR INFORMATION

Corresponding Authors

Jijie Huang − *School of Materials, Sun Yat-sen University, Guangzhou, Guangdong 510275, China*; Email: huangjj83@mail.sysu.edu.cn

Haiyan Wang − *School of Materials Engineering and School of Electrical and Computer Engineering, Purdue University, West Lafayette, Indiana 47907, United States*; orcid.org/0000-0002-7397-1209; Email: hwang00@purdue.edu

Authors

Di Zhang − *School of Materials Engineering, Purdue University, West Lafayette, Indiana 47907, United States*

Juncheng Liu − *School of Materials Engineering, Purdue University, West Lafayette, Indiana 47907, United States*

Hongyi Dou − *School of Materials Engineering, Purdue University, West Lafayette, Indiana 47907, United States*

Complete contact information is available at: https://pubs.acs.org/10.1021/acsami.1c14699

Notes

The authors declare no competing financial interest.

ACKNOWLEDGMENTS

This work was supported by the U.S. National Science Foundation (DMR-1565822 and DMR-2016453). D.Z. and H.W. acknowledge the support from the Office of Naval Research under contract no. N00014-20-1-2043 for TEM effort. J.H. acknowledges the support from Guangdong Basic and Applied Basic Research Foundation (2019A1515111029).

REFERENCES

(1) Kools, J. C. S. Exchange-Biased Spin-Valves for Magnetic Storage. *IEEE Trans. Magn.* **1996**, *32*, 3165−3184.

(2) Allibe, J.; Fusil, S.; Bouzehouane, K.; Daumont, C.; Sando, D.; Jacquet, E.; Deranlot, C.; Bibes, M.; Barthélémy, A. Room Temperature Electrical Manipulation of Giant Magnetoresistance in Spin Valves Exchange-Biased with $BiFeO_3$. *Nano Lett.* **2012**, *12*, 1141−1145.

(3) Jovičević Klug, M.; Thormählen, L.; Röbisch, V.; Toxværd, S. D.; Höft, M.; Knöchel, R.; Quandt, E.; Meyners, D.; McCord, J. Antiparallel Exchange Biased Multilayers for Low Magnetic Noise Magnetic Field Sensors. *Appl. Phys. Lett.* **2019**, *114*, 192410.

(4) Wei, Z.; Sharma, A.; Nunez, A. S.; Haney, P. M.; Duine, R. A.; Bass, J.; MacDonald, A. H.; Tsoi, M. Changing Exchange Bias in Spin Valves with an Electric Current. *Phys. Rev. Lett.* **2007**, *98*, 116603.

(5) Chen, X.; Hochstrat, A.; Borisov, P.; Kleemann, W. Magnetoelectric Exchange Bias Systems in Spintronics. *Appl. Phys. Lett.* **2006**, *89*, 202508.

(6) Ali, M.; Adie, P.; Marrows, C. H.; Greig, D.; Hickey, B. J.; Stamps, R. L. Exchange Bias Using a Spin Glass. *Nat. Mater.* **2007**, *6*, 70−75.

(7) Fan, Y.; Smith, K. J.; Lüpke, G.; Hanbicki, A. T.; Goswami, R.; Li, C. H.; Zhao, H. B.; Jonker, B. T. Exchange Bias of the Interface Spin System at the Fe/MgO Interface. *Nat. Nanotechnol.* **2013**, *8*, 438−444.

(8) Wu, S. M.; Cybart, S. A.; Yu, P.; Rossell, M. D.; Zhang, J. X.; Ramesh, R.; Dynes, R. C. Reversible Electric Control of Exchange Bias in a Multiferroic Field-Effect Device. *Nat. Mater.* **2010**, *9*, 756−761.

(9) Dobrynin, A. N.; Givord, D. Exchange Bias in a Co/CoO/Co Trilayer with Two Different Ferromagnetic-Antiferromagnetic Interfaces. *Phys. Rev. B: Condens. Matter Mater. Phys.* **2012**, *85*, 014413.

(10) Gibert, M.; Zubko, P.; Scherwitzl, R.; Íñiguez, J.; Triscone, J.-M. Exchange Bias in $LaNiO_3$-$LaMnO_3$ Superlattices. *Nat. Mater.* **2012**, *11*, 195−198.

(11) Leighton, C.; Fitzsimmons, M. R.; Hoffmann, A.; Dura, J.; Majkrzak, C. F.; Lund, M. S.; Schuller, I. K. Thickness-Dependent Coercive Mechanisms in Exchange-Biased Bilayers. *Phys. Rev. B: Condens. Matter Mater. Phys.* **2002**, *65*, 064403.

(12) Radu, F.; Abrudan, R.; Radu, I.; Schmitz, D.; Zabel, H. Perpendicular Exchange Bias in Ferrimagnetic Spin Valves. *Nat. Commun.* **2012**, *3*, 715.

(13) Ikeda, S.; Miura, K.; Yamamoto, H.; Mizunuma, K.; Gan, H. D.; Endo, M.; Kanai, S.; Hayakawa, J.; Matsukura, F.; Ohno, H. A Perpendicular-anisotropy CoFeB-MgO Magnetic Tunnel Junction. *Nat. Mater.* **2010**, *9*, 721−724.

(14) Pan, C.; An, H.; Harumoto, T.; Zhang, Z.; Nakamura, Y.; Shi, J. Control of the Perpendicular Magnetic Anisotropy and Perpendicular Exchange Bias in $CoPt/CoO_x$ Thin Films. *J. Magn. Magn. Mater.* **2019**, *484*, 320−323.

(15) Maat, S.; Takano, K.; Parkin, S. S.; Fullerton, E. E. Perpendicular Exchange Bias of Co/Pt Multilayers. *Phys. Rev. Lett.* **2001**, *87*, 087202.

(16) Huang, J.; MacManus-Driscoll, J. L.; Wang, H. New Epitaxy Paradigm in Epitaxial Self-Assembled Oxide Vertically Aligned Nanocomposite Thin Films. *J. Mater. Res.* **2017**, *32*, 4054−4066.

(17) Sun, X.; MacManus-Driscoll, J. L.; Wang, H. Spontaneous Ordering of Oxide-Oxide Epitaxial Vertically Aligned Nanocomposite Thin Films. *Annu. Rev. Mater. Res.* **2020**, *50*, 229−253.

(18) Huang, J.; Li, W.; Yang, H.; MacManus-Driscoll, J. L. Tailoring Physical Functionalities of Complex Oxides by Vertically Aligned Nanocomposite Thin-Film Design. *MRS Bull.* **2021**, *46*, 159−167.

(19) Ning, X.; Wang, Z.; Zhang, Z. Large, Temperature-tunable Low-field Magnetoresistance in $La_{0.7}Sr_{0.3}MnO_3$:NiO Nanocomposite Films Modulated by Microstructures. *Adv. Funct. Mater.* **2014**, *24*, 5393−5401.

(20) Fan, M.; Zhang, W.; Jian, J.; Huang, J.; Wang, H. Strong Perpendicular Exchange Bias in Epitaxial $La_{0.7}Sr_{0.3}MnO_3$:$LaFeO_3$ Nanocomposite Thin Films. *APL Mater.* **2016**, *4*, 076105.

(21) Wu, R.; Yun, C.; Wang, X.; Lu, P.; Li, W.; Lin, Y.; Choi, E.-M.; Wang, H.; MacManus-Driscoll, J. L. All-oxide Nanocomposites to Yield Large, Tunable Perpendicular Exchange Bias above Room Temperature. *ACS Appl. Mater. Interfaces* **2018**, *10*, 42593−42602.

(22) Zhang, W.; Chen, A.; Jian, J.; Zhu, Y.; Chen, L.; Lu, P.; Jia, Q.; MacManus-Driscoll, J. L.; Zhang, X.; Wang, H. Strong Perpendicular Exchange Bias in Epitaxial $La_{0.7}Sr_{0.3}MnO_3$:$BiFeO_3$ Nanocomposite Films through Vertical Interfacial Coupling. *Nanoscale* **2015**, *7*, 13808−13815.

(23) Huang, J.; Gellatly, A.; Kauffmann, A.; Sun, X.; Wang, H. Exchange Bias Effect along Vertical Interfaces in $La_{0.7}Sr_{0.3}MnO_3$:NiO Vertically Aligned Nanocomposite Thin Films Integrated on Silicon Substrates. *Cryst. Growth Des.* **2018**, *18*, 4388−4394.

(24) Huang, J.; Wang, H.; Wang, X.; Gao, X.; Liu, J.; Wang, H. Exchange Bias in a $La_{0.67}Sr_{0.33}MnO_3$/NiO Heterointerface Integrated on a Flexible Mica Substrate. *ACS Appl. Mater. Interfaces* **2020**, *12*, 39920−39925.

(25) Huang, Q. J.; Cheng, Y.; Liu, X. J.; Xu, X. D.; Zhang, S. Y. Study of the Elastic Constants in a $La_{0.6}Sr_{0.4}MnO_3$ Film by Means of Laser-generated Ultrasonic Wave Method. *Ultrasonics* **2006**, *44*, e1223−e1227.

(26) Gaillac, R.; Pullumbi, P.; Coudert, F.-X. ELATE: An Open-source Online Application for Analysis and Visualization of Elastic Tensors. *J. Phys.: Condens. Matter* **2016**, *28*, 275201.

(27) Fang, Z.; Solovyev, I. V.; Terakura, K. Phase Diagram of Tetragonal Manganites. *Phys. Rev. Lett.* **2000**, *84*, 3169.

(28) Li, Y.-Y. Magnetic Moment Arrangements and Magnetocrystalline Deformations in Antiferromagnetic Compounds. *Phys. Rev.* **1955**, *100*, 627−631.

(29) Li, J.; Arenholz, E.; Meng, Y.; Tan, A.; Park, J.; Jin, E.; Son, H.; Wu, J.; Jenkins, C. A.; Scholl, A.; Zhao, H.; Hwang, C.; Qiu, Z. Continuous Spin Reorientation Transition in Epitaxial Antiferromagnetic NiO Thin Films. *Phys. Rev. B: Condens. Matter Mater. Phys.* **2011**, *84*, 012406.

(30) Urushibara, A.; Moritomo, Y.; Arima, T.; Asamitsu, A.; Kido, G.; Tokura, Y. Insulator-Metal Transition and Giant Magnetoresistance in $La_{1-x}Sr_xMnO_3$. *Phys. Rev. B: Condens. Matter Mater. Phys.* **1995**, *51*, 14103.

(31) Chen, X. J.; Soltan, S.; Zhang, H.; Habermeier, H.-U. Strain Effect on Electronic Transport and Ferromagnetic Transition Temperature in $La_{0.9}Sr_{0.1}MnO_3$ Thin Films. *Phys. Rev. B: Condens. Matter Mater. Phys.* **2002**, *65*, 174402.

(32) Rao, R. A.; Lavric, D.; Nath, T. K.; Eom, C. B.; Wu, L.; Tsui, F. Three-dimensional Strain States and Crystallographic Domain Structures of Epitaxial Colossal Magnetoresistive $La_{0.8}Ca_{0.2}MnO_3$ Thin Films. *Appl. Phys. Lett.* **1998**, *73*, 3294−3296.

(33) Kumari, S.; Mottaghi, N.; Huang, C.-Y.; Trappen, R.; Bhandari, G.; Yousefi, S.; Cabrera, G.; Seehra, M. S.; Holcomb, M. B. Effects of Oxygen Modification on the Structural and Magnetic Properties of Highly Epitaxial $La_{0.7}Sr_{0.3}MnO_3$ (LSMO) Thin Films. *Sci. Rep.* **2020**, *10*, 3659.

(34) Kodama, R. H.; Makhlouf, S. A.; Berkowitz, A. E. Finite Size Effects in Antiferromagnetic NiO Nanoparticles. *Phys. Rev. Lett.* **1997**, *79*, 1393−1396.

(35) Sugiyama, I.; Shibata, N.; Wang, Z.; Kobayashi, S.; Yamamoto, T.; Ikuhara, Y. Ferromagnetic Dislocations in Antiferromagnetic NiO. *Nat. Nanotechnol.* **2013**, *8*, 266−270.

(36) Ali, M.; Marrows, C. H.; Al-Jawad, M.; Hickey, B. J.; Misra, A.; Nowak, U.; Usadel, K. D. Antiferromagnetic Layer Thickness Dependence of the IrMn/Co Exchange-Bias System. *Phys. Rev. B: Condens. Matter Mater. Phys.* **2003**, *68*, 214420.

(37) Morales, R.; Basaran, A. C.; Villegas, J. E.; Navas, D.; Soriano, N.; Mora, B.; Redondo, C.; Batlle, X.; Schuller, I. K. Exchange-Bias Phenomenon: The Role of the Ferromagnetic Spin Structure. *Phys. Rev. Lett.* **2015**, *114*, 097202.

(38) Lin, P.-H.; Yang, B.-Y.; Tsai, M.-H.; Chen, P.-C.; Huang, K.-F.; Lin, H.-H.; Lai, C.-H. Manipulating Exchange Bias by Spin-Orbit Torque. *Nat. Mater.* **2019**, *18*, 335−341.

https://doi.org/10.1021/acsami.1c14699
ACS Appl. Mater. Interfaces 2021, 13, 50141−50148

(39) Shi, X.; Mi, W.; Zhang, Q.; Zhang, X. Bending Strain Tailored Exchange Bias in Epitaxial NiMn/γ'-Fe_4N Bilayers. *Appl. Phys. Lett.* **2020**, *117*, 132401.
(40) Sun, X.; Huang, J.; Jian, J.; Fan, M.; Wang, H.; Li, Q.; Mac Manus-Driscoll, J. L.; Lu, P.; Zhang, X.; Wang, H. Three-Dimensional Strain Engineering in Epitaxial Vertically Aligned Nanocomposite Thin Films with Tunable Magnetotransport Properties. *Mater. Horiz.* **2018**, *5*, 536−544.
(41) Huang, J.; Wang, X.; Li, D.; Jin, T.; Lu, P.; Zhang, D.; Lin, P. T.; Chen, H. T.; Narayan, J.; Zhang, X.; Wang, H. 3D Hybrid Plasmonic Framework with Au Nanopillars Embedded in Nitride Multilayers Integrated on Si. *Adv. Mater. Interfaces* **2020**, *7*, 2000493.

https://doi.org/10.1021/acsami.1c14699
ACS Appl. Mater. Interfaces 2021, 13, 50141−50148